Power Electronic Systems
Laboratory

Proceedings of the IEEE International Electric Machines & Drives Conference (IEMDC 2017), Miami, FL, USA, May 21-24, 2017

A High Speed Millimeter-Scale Slotless Bearingless Slice Motor

M. Schuck,
A. Da Silva Fernandes,
D. Steinert,
J. W. Kolar

Eidgenössische Technische Hochschule Zürich
Swiss Federal Institute of Technology Zurich

A High Speed Millimeter-Scale Slotless Bearingless Slice Motor

Marcel Schuck[1], André Da Silva Fernandes[1], Daniel Steinert[2], Johann W. Kolar[1]
[1]Power Electronic Systems Laboratory, ETH Zurich, Zurich, Switzerland, schuck@lem.ee.ethz.ch
[2]Levitronix GmbH, Zurich, Switzerland

***Abstract*—Recent developments in electrical drive systems have shown a trend toward higher power densities at increased rotational speeds with application areas in high speed spindles, turbocompressors, flywheels and reaction wheels as well as optical systems. As conventional ball bearings suffer from excessive wear and decreased reliability at such speeds, contactless magnetic levitation offers an interesting alternative. This work presents the concept, design and implementation of a millimeter-scale bearingless slice motor featuring a rotor diameter of 4 mm. To the knowledge of the authors, this is the smallest published bearingless motor to date. The slotless stator topology is optimized by means of 3D finite element method electromagnetic simulations. Initial experimental results demonstrate a rotational speed of 160 000 rpm at losses below 1 W.**

Keywords — bearingless machine, high rotational speed, millimeter scale, slice motor, slotless.

I. Introduction

In recent years, there has been a trend in electrical drive systems toward higher rotational speeds to increase their power density [1], [2]. This development has been fueled by application areas such as turbocompressors [3], machining spindles [4], flywheels and reaction wheels [5], [6], as well as generators for micro gas turbines [7]. Some applications, such as rotating mirror optical systems [8], directly require very high rotational speeds.

This has led to miniaturization of electric machines with rotational speeds reaching levels at which the application of conventional ball bearings entails significant disadvantages, such as excessive wear, decreased reliability and a shortened lifetime. As a consequence, frictionless magnetic bearings, in which the rotor is levitated and rotated without any mechanical contact to the stator, can beneficially be applied to such machines. The advantage achieved by the use of magnetic bearings depends on the type of mechanical contact to the rotor as required by the considered application.

While a number of studies, such as [9], have concentrated on the benefits of contactless magnetic bearings in high purity or harsh environments, this work is focused on their potential in high speed electrical drive systems. An overview of systems employing magnetic bearings with published *measured results* of rotational speeds beyond 100 000 rpm is shown in Fig. 1. In [4], a spindle reaching 150 000 rpm for mechanical drilling is presented, which employs two separate (non-integrated) reluctance-force-based active magnetic bearings (AMB). The same topology was used in [10] to reach 121 000 rpm. A self-bearing machine, which uses separate windings for the drive and magnetic bearing but a common iron circuit has been presented in [11]. This motor uses a long cylindrical shaft rotor (length ≫ diameter) and is capable of reaching 500 000 rpm, which is the highest rotational speed achieved by a synchronous machine employing magnetic bearings to date. Besides the mechanical strength of the rotor, the achievable rotational speed is also limited by the critical frequency at which bending of the rotor occurs [12], [13]. In such machines it is necessary to actively stabilize all degrees of freedom, which not only requires a comparatively high control effort and number of AMBs but also complicates the rotor construction, thereby limiting its miniaturization potential.

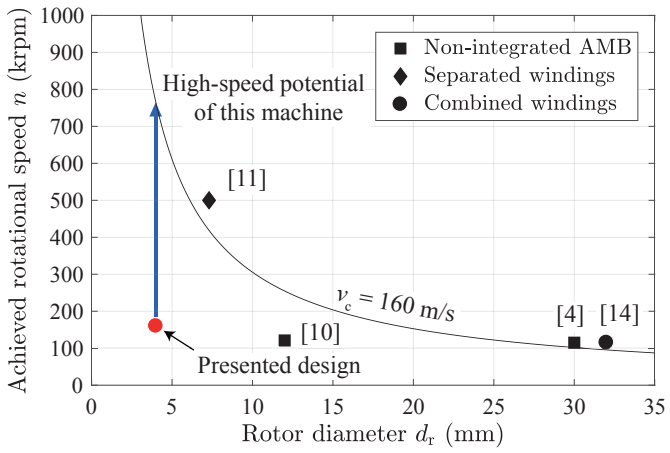

Fig. 1: Overview of high speed electric drive systems employing magnetic bearings with measured rotational speeds above 100 000 rpm.

To overcome these limitations, a bearingless slice motor topology as shown in Fig. 2 can be used in which the degrees of freedom in axial and tilting directions are passively stabilized, only requiring an AMB in radial direction [9]. Moreover, the critical frequencies (bending modes) of the short rotor are well above the mechanical limit due to centrifugal loading. This has been demonstrated in [14], where a rotor was accelerated to 115 000 rpm until mechanical failure occurred (cf. Fig. 1). In [15] a rotational speed of 140 000 rpm was reached, but no information about the rotor diameter is provided.

To demonstrate the feasibility of downscaling and the accompanying high speed potential of this topology, the design

978-1-5090-4281-4/17/$31.00 ©2017 IEEE

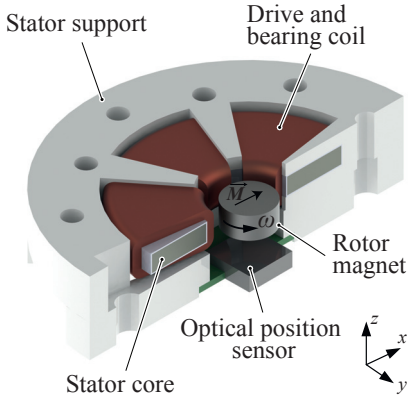

Fig. 2: Topology of the presented high speed millimeter-scale slotless bearingless slice motor.

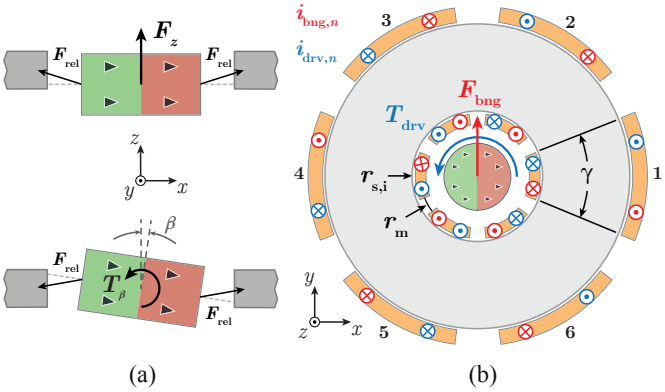

Fig. 3: Passive stiffnesses (a) and active torque and radial bearing force generation (b) in the chosen motor topology.

and implementation of a millimeter-scale bearingless slice motor is outlined in this work.

Obtaining sufficient passive stiffnesses is particularly challenging for small scale systems and the achievable drive torque is significantly lower than in a motor with a shaft rotor. In order to actively control the rotor in radial direction, its position needs to be measured, which is demanding due to the confined space available around the rotor. The low inertia of the rotor, with its mass being in the range of a few hundred milligrams, requires fast and accurate control in order to facilitate stable levitation.

These challenges are systematically addressed in this paper. Potential application areas of the proposed motor design are in small size flywheels and reaction wheels, optical systems as well as hyper-gravity science.

The remainder of this paper is organized as follows: Section II describes the operating principle of the employed motor topology, while Section III briefly outlines the losses occurring in the motor. Section IV details the mechanical and electrical design of the motor by means of 3D finite element method (FEM) electromagnetic simulations as well as the used sensor systems. Experimental results obtained from a prototype that verify the performance of the machine are presented in Section V. Finally, Section VI concludes the paper.

II. Operating Principle

A slotless topology referring to a ring-shaped stator without teeth to guide the magnetic flux towards the rotor is used in this work. It is particularly suitable for operation at high rotational speeds, as it features reduced eddy current losses due to the absence of stator harmonics. The coils are wound toroidally around the stator core. The operating principle of the slotless bearingless slice motor has been described in [14] and [16]. For a better understanding of the subsequent simulations and experiments, the key principle and properties are discussed in this section.

A. Passive Stability

Due to the disc shape (height $<$ diameter) of the diametrically-magnetized permanent magnet rotor and a similar height of the ferromagnetic stator core, the rotor is passively stable in axial (z) and tilting (α, β) directions. Axial displacement or tilting causes an increase of the magnetic air gap length, resulting in a restoring reluctance force or torque as shown in Fig. 3(a), respectively. The positive passive stiffnesses

$$k_z = -\frac{\mathrm{d}F_z}{\mathrm{d}z},\ k_\alpha = -\frac{\mathrm{d}T_\alpha}{\mathrm{d}\alpha} \text{ and } k_\beta = -\frac{\mathrm{d}T_\beta}{\mathrm{d}\beta} \tag{1}$$

can be defined, where α and β denote the tilting angles around the d (magnetization direction) and q (perpendicular to the magnetization direction) axis of the rotor, respectively.

Contrarily, the unstable and, therefore, negative passive radial stiffnesses along the d and q axis are defined as

$$k_d = -\frac{\mathrm{d}F_d}{\mathrm{d}d} \quad \text{and} \quad k_q = -\frac{\mathrm{d}F_q}{\mathrm{d}q}, \tag{2}$$

respectively. For a rotor with a pole pair number p_{pm} of 1, such as used in this work, $k_\alpha < k_\beta$ and $k_q < k_d$ holds.

B. Active Radial Bearing and Drive

The rotor has to be stabilized actively in radial direction by an AMB. To generate a radial force, a magnetic field with a pole pair number of $p_{\mathrm{bng}} = p_{\mathrm{pm}}+1 = 2$ needs to be generated, which is achieved by applying a bearing current of magnitude $\hat{I}_{\mathrm{bng}}$ in the same direction to coils on opposite sides of the stator as shown in Fig. 3(b).

To provide a semi analytic expression of the bearing force, the flux density generated by the rotor in the air gap is approximated by

$$\vec{B}_{\mathrm{pm}} \approx \hat{B}_{\mathrm{pm}} \cos(\varphi - \vartheta)\vec{e}_r, \tag{3}$$

where φ, ϑ denote the polar angle in cylinder coordinates and the rotor angle, respectively. This approximation is justified by the constant magnetic air gap length δ_{mag} being distinctly smaller than the distance between the magnetic poles along

the circumference of the rotor. The magnetic field in the air gap generated by the stator coils can be written as

$$\vec{B}_{\mathrm{s}} \approx \hat{B}_{\mathrm{s}} \cos(2\varphi - \vartheta - \Delta\varphi)\vec{e}_r, \tag{4}$$

where $\Delta\varphi$ denotes a phase shift between the rotor angle and the applied coil currents. The radial bearing force is then obtained as

$$\vec{F}_{\mathrm{bng}} = \underbrace{h \iint_{A_{\mathrm{cu}}} (\vec{J}_{\mathrm{bng}} \times \vec{B}_{\mathrm{pm}}) \mathrm{d}A}_{\text{Lorentz force}} + \underbrace{\frac{h r_{\mathrm{s,i}}}{2\mu_0} \int_0^{2\pi} (\vec{B}_{\mathrm{pm}} + \vec{B}_{\mathrm{s}})^2 \mathrm{d}\varphi}_{\text{Maxwell force}}, \tag{5}$$

where A_{cu}, J_{bng}, h, $r_{\mathrm{s,i}}$ denote the cross sectional area of the coils, current density in the coils, height of the air gap, and the inner radius of the stator (cf. Fig. 3(b)), respectively. By solving (5), the bearing force can be rewritten in Cartesian coordinates as

$$\vec{F}_{\mathrm{bng}} = k_{\mathrm{F}} \cdot \hat{I}_{\mathrm{bng}} \begin{bmatrix} \cos(\Delta\varphi) \\ \sin(\Delta\varphi) \end{bmatrix} = k_{\mathrm{F}} \cdot \begin{bmatrix} \hat{I}_{\mathrm{bng},x} \\ \hat{I}_{\mathrm{bng},y} \end{bmatrix}. \tag{6}$$

Using a line current density model and only considering its fundamental component, an expression for k_{F} can be found as

$$k_{\mathrm{F}} = \frac{Nh}{2} \left(\frac{3\sin(\gamma)}{\gamma} + \frac{r_{\mathrm{s,i}} \pi k_{\mathrm{B}}}{\mu_0} \right) \hat{B}_{\mathrm{pm}}, \tag{7}$$

with γ, N being the angle occupied by a single coil and number of turns per coil, respectively. The factor $k_{\mathrm{B}} = \hat{B}_{\mathrm{s}}/(N\hat{I}_{\mathrm{bng}})$ is a measure for how much stator field is generated per current and can be determined through simulations or analytical calculations [17].

To generate a drive torque, a magnetic field with a pole pair number of $p_{\mathrm{drv}} = p_{\mathrm{pm}} = 1$ is generated by applying a drive current of magnitude $\hat{I}_{\mathrm{drv}}$ in opposite directions to coils on opposite sides of the stator as shown in Fig. 3(b). The drive torque, which is only caused by the Lorentz force, can be calculated as

$$\vec{T}_{\mathrm{drv}} = h \iint_{A_{\mathrm{cu}}} \vec{r} \times \left(\vec{J}_{\mathrm{drv}} \times \vec{B}_{\mathrm{pm}} \right) \mathrm{d}A, \tag{8}$$

resulting in $T = k_{\mathrm{T}} \cdot \hat{I}_{\mathrm{drv}}$. The torque constant k_{T} is obtained to be

$$k_{\mathrm{T}} = \frac{6Nhr_{\mathrm{m}}}{\gamma} \sin\left(\frac{\gamma}{2}\right) \hat{B}_{\mathrm{pm}}, \tag{9}$$

with r_{m} being the mean radius of the coils. For the design of the motor, it is desirable for k_{F} and k_{T} to be as high as possible for achieving a high bearing force and torque, respectively. The drive and bearing currents can be written as two virtual three phase systems as

$$\begin{bmatrix} i_{\mathrm{bng},A} \\ i_{\mathrm{bng},B} \\ i_{\mathrm{bng},C} \end{bmatrix} = K(\vartheta) \cdot \begin{bmatrix} \hat{I}_{\mathrm{bng},x} \\ \hat{I}_{\mathrm{bng},y} \end{bmatrix} \quad \begin{bmatrix} i_{\mathrm{drv},A} \\ i_{\mathrm{drv},B} \\ i_{\mathrm{drv},C} \end{bmatrix} = K(\vartheta) \cdot \begin{bmatrix} 0 \\ \hat{I}_{\mathrm{drv}} \end{bmatrix}, \tag{10}$$

where

$$K(\vartheta) = -\begin{bmatrix} \sin(\vartheta) & \cos(\vartheta) \\ \sin(\vartheta - \frac{2\pi}{3}) & \cos(\vartheta - \frac{2\pi}{3}) \\ \sin(\vartheta + \frac{2\pi}{3}) & \cos(\vartheta + \frac{2\pi}{3}) \end{bmatrix} \tag{11}$$

denotes the Park (dq) transformation matrix between the rotor and stator coordinate systems. To make best use of the tightly confined space in the air gap, combined windings for drive torque and bearing force generation (cf. [14], [16]) are used in the presented motor. Consequently, the coil currents are calculated as

$$\begin{aligned} i_1 &= i_{\mathrm{bng},A} + i_{\mathrm{drv},A} & i_4 &= i_{\mathrm{bng},A} - i_{\mathrm{drv},A} \\ i_2 &= i_{\mathrm{bng},B} - i_{\mathrm{drv},C} & i_5 &= i_{\mathrm{bng},B} + i_{\mathrm{drv},C} \\ i_3 &= i_{\mathrm{bng},C} + i_{\mathrm{drv},B} & i_6 &= i_{\mathrm{bng},C} - i_{\mathrm{drv},B}, \end{aligned} \tag{12}$$

where the coils are labeled as shown in Fig. 3(b). These currents can be divided into two physical three phase systems with floating star points, as

$$i_1 + i_3 + i_5 = 0 \quad \text{and} \quad i_2 + i_4 + i_6 = 0 \tag{13}$$

hold.

III. Losses

The losses in the considered slotless machine topology mainly consist of copper losses P_{cu} in the windings, core losses P_{fe} in the ferromagnetic material of the stator core, and air friction losses P_{air} at the surfaces of the rotor due to high speed rotation. Rotor losses caused by induced eddy currents are generally considered to be low in slotless machines [18], [19] and are not examined further here.

A. Copper Losses

The copper losses can be subdivided into conduction losses $P_{\mathrm{cu,R}}$ due to the ohmic resistance R_{dc} of the windings and eddy current losses $P_{\mathrm{cu,ed}}$ due to the alternating magnetic field penetrating the windings. As the field generated by the stator is small compared to that of the rotor, $P_{\mathrm{cu,ed}}$ can be obtained in good approximation by only considering $\hat{B}_{\mathrm{pm}}$. For the same reason, copper losses due to the proximity effect can be neglected. Moreover, skin effect losses can be neglected due to the small wire diameters used. Based on these assumptions, the copper losses in coil k can be calculated as [20]

$$P_{\mathrm{cu},k} = \underbrace{I_k^2 R_{\mathrm{dc}}}_{P_{\mathrm{cu,R}}} + \underbrace{\frac{\pi^3 N p d_{\mathrm{cu}}^4 \sigma_{\mathrm{cu}} f^2}{32} \int_L \hat{B}_{\mathrm{pm}}^2 \mathrm{d}l}_{P_{\mathrm{cu,ed}}}, \tag{14}$$

where, p, d_{cu}, σ_{cu}, f denote the number of parallel conductors per coil, the wire diameter, the conductivity of copper and the rotational frequency, respectively. The integration along the complete wire length L of each turn is performed to account for fluctuations of $\hat{B}_{\mathrm{pm}}$ along the axial direction of the machine and to consider that parts of the windings above and below the air gap are also penetrated by the rotor field [21]. For slotless machines with shaft rotors, the integral term is frequently approximated by $\hat{B}_{\mathrm{pm}}^2 h$ [22].

B. Core Losses

Losses in the stator core are mostly due to the magnetic field of the rotor and are calculated using the Steinmetz equation as an integral over the core volume V_{fe}

$$P_{\mathrm{fe}} = \int_{V_{\mathrm{fe}}} C_{\mathrm{m}} f^{\alpha} \hat{B}^{\beta} \mathrm{d}V, \tag{15}$$

where the Steinmetz coefficients of the used Metglas 2605SA1 amorphous alloy stator core material [23] were obtained to be $C_{\mathrm{m}} = 1.90\,\mathrm{W/m^3}$, $\alpha = 1.45$, and $\beta = 1.67$.

C. Air Friction Losses

For a disc-shaped rotor, such as the one used in this study, the air friction losses can be expressed as

$$P_{\mathrm{air}} = C_{\mathrm{f}} \rho_{\mathrm{air}} \omega^3 \left(\pi h_{\mathrm{r}} \left(\frac{d_{\mathrm{r}}}{2} \right)^4 + \left(\frac{d_{\mathrm{r}}}{2} \right)^5 \right), \tag{16}$$

where ρ_{air} is the mass density of air and h_{r} is the rotor height. The first and second summand in parentheses correspond to the contributions of the cylindrical and the two face surfaces of the rotor, respectively. It can be seen that these losses scale cubically with $\omega = 2\pi n/60$, making them particularly relevant for high speed machines, and that the small rotor diameter has a favorable influence. C_{f} denotes an empirically obtained friction coefficient dependent on the Reynolds number, which is a measure for how laminar or turbulent the flow is. As the value of C_{f} varies significantly with the conditions under which it was obtained, accurate prediction of the air friction losses proves to be difficult. The most conservative value for C_{f} found in the literature [24] was used in this study to provide an estimate which is considered to be an upper bound.

IV. Motor Design

This section outlines the mechanical and electrical design of the proposed millimeter-scale bearingless disc drive and describes the used sensor systems.

A. Rotor

The occurring stress inside the rotor due to centrifugal loading depends on its rotational speed and material density ρ_{r}. The stress that the material can withstand is determined by its tensile strength σ_{s}. Therefore, the achievable rotational speed is governed by the tensile strength to density ratio of the rotor material. A measure for this property is the achievable circumferential speed v_{c}, which is independent of the rotor diameter. The maximum stress occurs at the center of the disc-shaped rotor and is pointed in radial direction. Its value can be calculated as

$$\sigma_{\max} = \frac{3+\nu}{8} \rho_{\mathrm{r}} v_{\mathrm{c}}^2, \tag{17}$$

where ν denotes the Poisson's ratio of the material and $v_{\mathrm{c}} = \omega d_{\mathrm{r}}/2$ [25]. The rotor consists of an N45 grade NdFeB permanent magnet, for which the values $\nu = 0.24$, $\rho_{\mathrm{r}} = 7\,500\,\mathrm{kg/m^3}$, and $\sigma_{\mathrm{s}} = 80\,\mathrm{MPa}$ are provided in the material datasheet. Using these values in the further considerations yields a maximum achievable circumferential speed of

$$v_{\max} = \sqrt{\frac{8\sigma_{\mathrm{s}}}{(3+\nu)\rho}} \approx 160\,\frac{\mathrm{m}}{\mathrm{s}}, \tag{18}$$

resulting in the curve added to Fig. 1. To increase this value, and thereby the achievable rotational speed, it is possible to prestress the rotor towards the insight by using a titanium sleeve [2] or to apply a carbon fiber bandage [14]. Due to the small geometry and the accompanying low mechanical tolerances, this has not been considered in this study.

A rotor diameter of $d_{\mathrm{r}} = 4\,\mathrm{mm}$ was chosen, for which the mechanical limit of the achievable rotational speed is given as $n_{\max} \approx 760\,000\,\mathrm{rpm}$ (cf. Fig. 1), corresponding to a fundamental frequency of the rotating drive field of 12.7 kHz. This rotor size still allows for mounting loads, such as small-scale rotating mirrors for optical systems [8]. The rotor height is constrained by the passive stability requirement of the magnetic bearing and was chosen as $h_{\mathrm{r}} = 2\,\mathrm{mm}$. Sufficiently well balanced permanent magnets of this size are readily available.

B. Stator

The stator core was optimized to provide high passive stiffnesses and good active properties for the chosen rotor geometry, where priority was given to the former. The optimization was carried out using 3D FEM electromagnetic simulations. Metglas 2605SA1 was used for the core material as it features lower core losses than conventional sheeted electrical steel, especially at high field frequencies. In an initial step, the height of the stator core was optimized to yield high values of k_z and k_α, while not compromising the torque and bearing force generation. The results are shown in Figs. 4 and 5, from which a stator core height of $h_{\mathrm{s}} = 1.5\,\mathrm{mm}$ was selected.

Further simulations were carried out assessing the effect of the inner stator core diameter. The results showed a rapid drop of the passive and active motor properties for an increase of $d_{\mathrm{s,i}}$, thus emphasizing the importance of choosing it as small as possible. This is particularly challenging for small scale machines, as the air gap does not easily scale down with the rest of the motor dimensions, resulting in the choice of $d_{\mathrm{s,i}} = 7.5\,\mathrm{mm}$. Consequently, the air gap length δ_{mag} is 1.75 mm, which amounts for about 44 % of the rotor diameter. The mechanical air gap length between the rotor and the inner stator wall is 0.5 mm and only 0.75 mm of radial space is available for the windings. To offer sufficiently small bending radii and flexibility for fitting into this narrow winding window and to limit high frequency copper losses, the coils consist of litz wire.

The dimensions of the designed motor are listed in Table I, and Table II lists the simulated electromechanical properties of the motor.

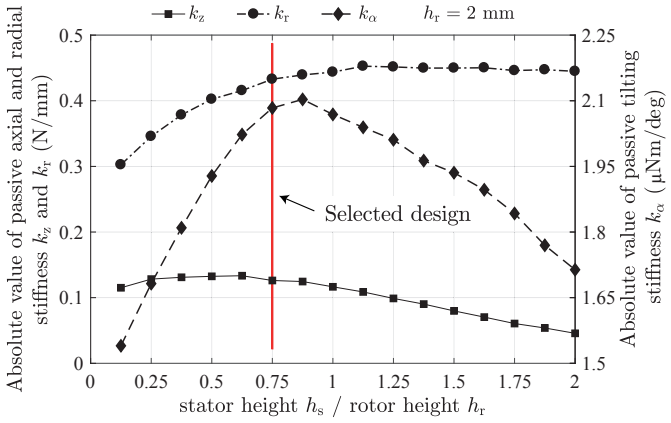

Fig. 4: Simulated passive stiffness parameters of the motor for varying heights of the stator core.

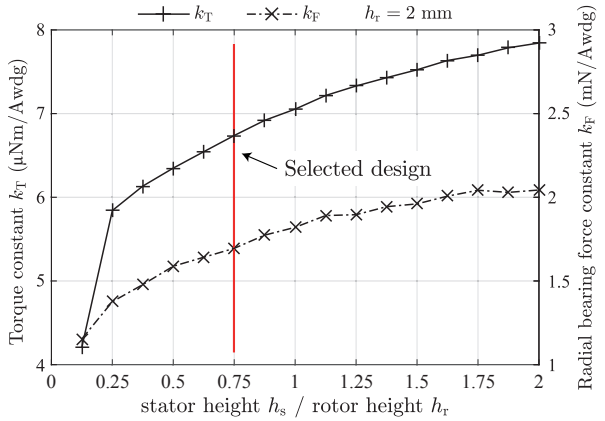

Fig. 5: Simulated torque and active radial bearing force constants for varying heights of the stator core.

TABLE I: Dimensions of the Prototype

Parameter		Value
Rotor diameter	d_r	4 mm
Rotor height	h_r	2 mm
Rotor mass	m_r	188 mg
Moment of inertia	J	$376 \cdot 10^{-12}$ kg m^2
Stator core height	h_s	1.5 mm
Magnetic airgap length	δ_{mag}	1.75 mm
Overall motor diameter	d_m	29 mm
Overall motor height	h_m	10 mm

C. Sensor Systems

The radial position and angle ϑ of the rotor have to be measured to facilitate active control of magnetic levitation and rotation. As shown in (10), the drive and bearing currents both have to be rotated dependent on ϑ. Placement of the required sensors is complicated by the small motor geometry.

Position sensor systems, such as the one presented in [10], cannot be used as the rotor is not long enough to be inserted through the excitation coil of an eddy current sensor. Therefore, the radial position is measured using an optical photo sensitive device (PSD) sensor, which is placed below the rotor as shown in Fig. 2 (cf. [26]). The sensor

TABLE II: Electromechanical Properties of the Prototype

Parameter		Value
Passive Properties		
Radial stiffness in d-axis	k_d	−0.43 N/mm
Radial stiffness in q-axis	k_q	−0.30 N/mm
Axial stiffness	k_z	0.13 N/mm
Tilting stiffness around d-axis	k_α	2.08 µNm/deg
Tilting stiffness around q-axis	k_β	4.06 µNm/deg
Active Properties		
Torque constant	k_T	6.7 µNm/Awdg
Radial bearing force constant	k_F	1.7 mN/Awdg

outputs four currents that are proportional to the centroid position of the incident light on its active area. A displacement of the rotor in radial direction results in a displacement of its shadow cast onto the sensor, which in turn affects the location of the centroid. To obtain a high contrast projection, an infrared LED is used to shine light onto the rotor from above. The sensitivity and bandwidth of this system are mainly dependent on the subsequent operational amplifier circuit used for signal conditioning. The latter was dimensioned to have a cutoff frequency of a few kilohertz, which is well above the radial dynamics of the rotor (a few hundred hertz) and allows for sufficient oversampling and filtering. The rotor angle is obtained by high bandwidth Hall sensors measuring the stray flux of the permanent magnet. The generated signals are sampled and fed into a digital controller hardware.

V. Experimental Results

An experimental prototype was implemented based on the results of Section IV. The rotor is a commercially available permanent magnet with pole pair number $p_r = 1$. All mechanical parts were manufactured using 3D printing technology and the stator core was fabricated using wire cutting. The rotor is levitated inside a hollow plastic cylinder to protect the stator windings. The six stator coils are connected to form two three phase systems, each with a separate floating star point. The employed power electronic converter for controlling the drive and bearing currents consists of six PWM-modulated switching half bridges with a dc-link voltage of 48 V. An annotated photograph of the implemented prototype and its rotor is shown in Fig. 6.

A. Rotational Speed

After stable levitation was attained, acceleration tests to a rotational speed of 160 000 rpm were conducted, for which the rotor flux signal measured by one Hall sensor is displayed in Fig. 7 (blue trace). The same figure also shows the measured position signal and the current in one of the coils at the same rotational speed. It can be seen that the position signal (green trace) is very stable. The observable high frequency noise component is electromagnetically coupled in from the switching of the power electronics and is not correlated to an actual movement of the rotor. This component is removed via digital filtering and does not affect the stability of the rotor. Contrarily, the obtained coil current (red trace) is not sufficiently accurate due to the high frequency of the drive

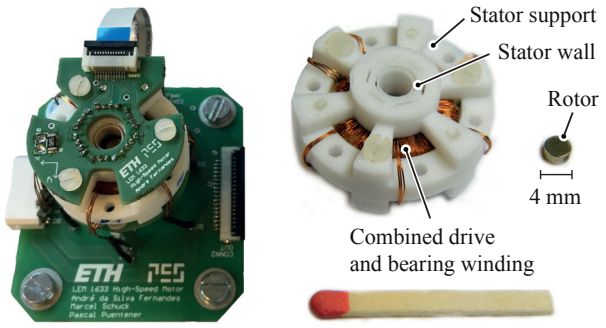

(a) (b)

Fig. 6: Implemented prototype (a) and annotated detail view of the stator and rotor with dimensional comparison to a match (b).

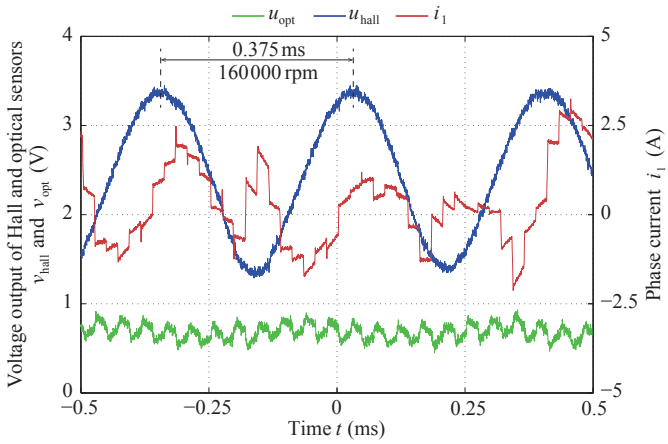

Fig. 7: Oscilloscope screenshot of relevant signals at a rotational speed of 160 000 rpm.

current required for such high rotational speeds (2.67 kHz at 160 000 rpm for $p_r = 1$) and causes the rotor to become unstable. This issue is caused by the employed off-the-shelf power electronics and controller, allowing for less than 10 PWM cycles per revolution of the rotor. Consequently, the sharp current jumps and significant deviation from an expected sinusoidal waveform observed in Fig. 7 result. To reach higher rotational speeds closer to the stress limit of the rotor at 760 000 rpm, a faster (e.g. FPGA-controlled) power electronic converter offering higher PWM switching frequency and shorter control loop times is required.

B. Levitation Stability

To assess the stability of magnetic levitation, the rotor position was logged during acceleration from 5 000 rpm to 162 000 rpm. The result is shown in Fig. 8, which also contains a depiction of the maximum allowable displacement, corresponding to the rotor touching the stator wall. It can be observed that the rotor orbit is larger for low rotational speeds, which is attributed to the relatively low tilting stiffnesses as obtained in Section IV. At higher rotational speeds the

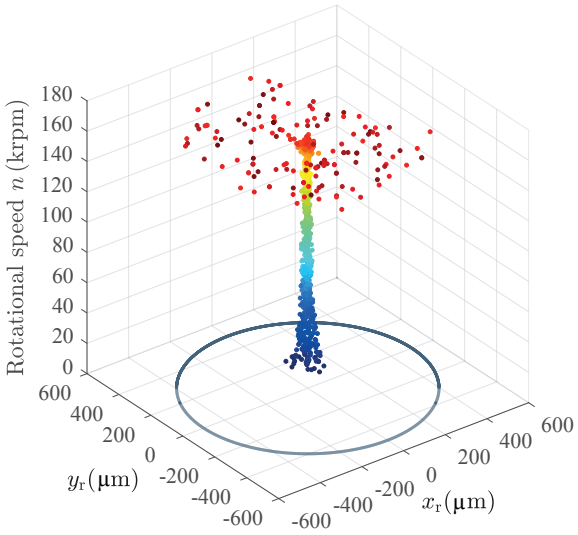

Fig. 8: Measured rotor orbit during acceleration to 162 000 rpm. The blue circle represents the maximum allowable displacement, at which the rotor touches the stator wall.

tilting movement is additionally stabilized by the angular momentum of the rotor, which limits displacements to values below 25 µm up to 160 000 rpm. At about 162 000 rpm the rotor becomes abruptly unstable due to the aforementioned controller limitations.

C. Losses

The losses were measured at the input terminals of the motor using a Yokogawa WT1804E high precision power analyzer. The rotational speed was increased in steps of 5 000 rpm from 10 000 rpm to 160 000 rpm and the measurement was taken after steady state had been reached. The motor losses were calculated from the four measured line to line voltages and currents as

$$P_{\text{meas}} = \overline{u_{15} i_1} + \overline{u_{35} i_3} + \overline{u_{26} i_2} + \overline{u_{46} i_4}, \tag{19}$$

where the indices denote the respective coil numbers. The result is shown in Fig. 9, which illustrates that the overall motor losses are below 1 W even for a rotational speed of 160 000 rpm. To separate the overall losses into their individual components, the models provided in Section III were used. The conduction losses in the coils were obtained by inserting the measured rms phase currents in (14). As expected, these losses constitute the highest portion of the overall losses, caused by the narrow winding window and the consequent small wire diameter. The core losses P_{fe} and eddy current losses in the coils $P_{\text{cu,ed}}$ are found to be at negligible levels. This is due to the relatively low magnitude of the flux density inside the stator core and the small wire diameter, respectively. The increasing portion of the losses that is not covered by the presented models is attributed to harmonic effects due to the low switching frequency of the converter (see current waveform in Fig. 7). The latter generate additional losses in the

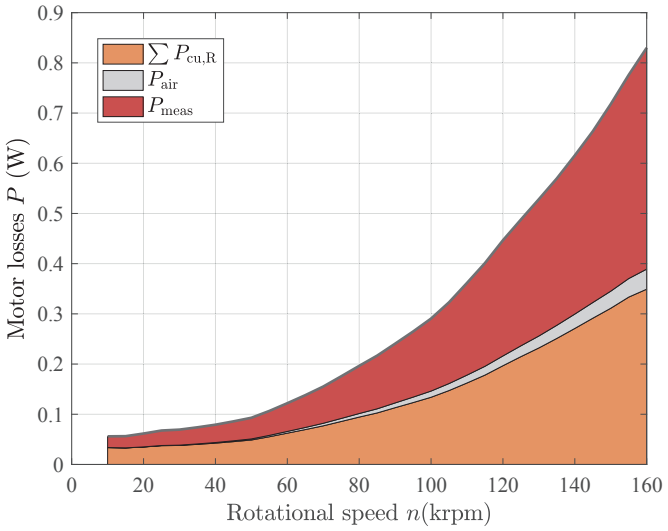

Fig. 9: Measured motor losses and separation into their components based on the presented loss models.

stator core, windings and rotor. Nevertheless, due to the low absolute losses, the motor is thermally stable with maximum temperatures of the windings, which are the hottest parts of the motor, below 45 °C after several minutes of operation at 160 000 rpm.

VI. Conclusion

The design and implementation of a millimeter-scale slotless bearingless slice motor has been presented. The employed rotor has a diameter of 4 mm and a height of 2 mm. To the knowledge of the authors, this is the smallest bearingless motor published to date. The chosen slotless topology is particularly well suited for high speed operation. A rotational speed of 160 000 rpm was reached at motor losses below 1 W, making the designed machine particularly interesting for low power applications such as optical systems. The rotational speed is currently constrained by the employed power electronic converter. By overcoming this limitation, the achievable rotational speed can be increased further toward the mechanical limit of the presented machine at 760 000 rpm.

Acknowledgment

The authors would like to thank Pascal Püntener for his help throughout the project.

References

[1] M. A. Rahman, A. Chiba, and T. Fukao, "Super high speed electrical machines - summary," in *Proc. IEEE Power Engineering Society General Meeting*, Jun. 2004, pp. 1272–1275 Vol.2.

[2] C. Zwyssig, J. Kolar, and S. Round, "Megaspeed drive systems: Pushing beyond 1 million r/min," *IEEE/ASME Trans. Mechatronics*, vol. 14, no. 5, pp. 564–574, 2009.

[3] D. Krahenbuhl, C. Zwyssig, H. Weser, and J. W. Kolar, "A miniature 500 000-r/min electrically driven turbocompressor," *IEEE Transactions on Industry Applications*, vol. 46, no. 6, pp. 2459–2466, Nov. 2010.

[4] M. Kimman, H. Langen, and R. M. Schmidt, "A miniature milling spindle with active magnetic bearings," *Mechatronics*, vol. 20, no. 2, pp. 224 – 235, 2010.

[5] J. Fausz, B. Wilson, C. Hall, D. Richie, and V. Lappas, "Survey of technology developments in flywheel attitude control and energy storage systems," *Journal of guidance, control, and dynamics*, vol. 32, no. 2, pp. 354–365, 2009.

[6] C. Zwyssig, T. Baumgartner, and J. W. Kolar, "High-speed magnetically levitated reaction wheel demonstrator," in *Proc. Int. Power Electronics Conf. (IPEC-Hiroshima 2014 - ECCE ASIA)*, May 2014, pp. 1707–1714.

[7] A. H. Epstein, "Millimeter-scale, micro-electro-mechanical systems gas turbine engines," *Transactions of the ASME-A-Engineering for Gas Turbines and Power*, vol. 126, no. 2, pp. 205–226, 2004.

[8] G. F. Marshall and G. E. Stutz, *Handbook of optical and laser scanning*. CRC Press, 2011.

[9] R. Schoeb and N. Barletta, "Principle and application of a bearingless slice motor," *JSME International Journal Series C Mechanical Systems, Machine Elements and Manufacturing*, vol. 40, no. 4, pp. 593–598, 1997.

[10] C. M. Zingerli, P. Imoberdorf, J. W. Kolar, and T. Nussbaumer, "Rotor position measurement for a magnetically levitated 500'000 rpm permanent magnet machine," in *Proc. IEEE Energy Conversion Congress and Exposition*, Sep. 2011, pp. 1778–1784.

[11] T. Baumgartner, R. M. Burkart, and J. W. Kolar, "Analysis and design of a 300-W 500 000-r/min slotless self-bearing permanent-magnet motor," *IEEE Transactions on Industrial Electronics*, vol. 61, no. 8, pp. 4326–4336, Aug. 2014.

[12] G. Schweitzer and E. Maslen, "Magnetic bearings, theory, design, and application," *Springer-Verlag, Heidelberg, Germany*, 2009.

[13] A. Borisavljevic, H. Polinder, and J. A. Ferreira, "On the speed limits of permanent-magnet machines," *IEEE Transactions on Industrial Electronics*, vol. 57, no. 1, pp. 220–227, Jan. 2010.

[14] H. Mitterhofer, W. Gruber, and W. Amrhein, "On the high speed capacity of bearingless drives," *IEEE Transactions on Industrial Electronics*, vol. 61, no. 6, pp. 3119–3126, Jun. 2014.

[15] S. Silber, J. Sloupensky, P. Dirnberger, M. Moravec, W. Amrhein, and M. Reisinger, "High-speed drive for textile rotor spinning applications," *IEEE Transactions on Industrial Electronics*, vol. 61, no. 6, pp. 2990–2997, Jun. 2014.

[16] D. Steinert, T. Nussbaumer, and J. W. Kolar, "Slotless bearingless disk drive for high-speed and high-purity applications," *IEEE Transactions on Industrial Electronics*, vol. 61, no. 11, pp. 5974–5986, Nov. 2014.

[17] P. D. Pfister and Y. Perriard, "Slotless permanent-magnet machines: General analytical magnetic field calculation," *IEEE Transactions on Magnetics*, vol. 47, no. 6, pp. 1739–1752, Jun. 2011.

[18] N. Bianchi, S. Bolognani, and F. Luise, "Potentials and limits of high-speed pm motors," *IEEE Transactions on Industry Applications*, vol. 40, no. 6, pp. 1570–1578, Nov. 2004.

[19] M. Markovic and Y. Perriard, "Analytical solution for rotor eddy-current losses in a slotless permanent-magnet motor: The case of current sheet excitation," *IEEE Transactions on Magnetics*, vol. 44, no. 3, pp. 386–393, Mar. 2008.

[20] P. N. Murgatroyd, "Calculation of proximity losses in multistranded conductor bunches," *Management and Education IEE Proceedings A-Physical Science, Measurement and Instrumentation*, vol. 136, no. 3, pp. 115–120, May 1989.

[21] D. Steinert, I. Kovacevic-Badstübner, T. Nussbaumer, and J. W. Kolar, "Loss investigation of slotless bearingless disk drives," in *Proc. IEEE Energy Conversion Congress and Exposition (ECCE)*, Sep. 2015, pp. 4418–4424.

[22] A. Borisavljevic, *Electromagnetic Modeling of Slotless PM Machines*. Springer Berlin Heidelberg, 2013, pp. 29–70.

[23] *2605SA1 Magnetic Alloy*, Metglas, 4 2011.

[24] J. W. Daily and R. E. Nece, "Chamber dimension effects on induced flow and frictional resistance of enclosed rotating disks," *ASME J. basic eng*, vol. 82, no. 1, pp. 217–230, 1960.

[25] A. I. Lurie, *Theory of elasticity*. Berlin: Springer, 2005.

[26] M. Schuck, D. Steinert, and J. W. Kolar, "Active radial magnetic bearing for an ultra-high speed motor," in *Proc. 18th European Conf. Power Electronics and Applications (EPE'16 ECCE Europe)*, Sep. 2016, pp. 1–10.